



Transient Water Vapor at Europa's South Pole

Lorenz Roth *et al.*

Science **343**, 171 (2014);

DOI: 10.1126/science.1247051

This copy is for your personal, non-commercial use only.

If you wish to distribute this article to others, you can order high-quality copies for your colleagues, clients, or customers by [clicking here](#).

Permission to republish or repurpose articles or portions of articles can be obtained by following the guidelines [here](#).

The following resources related to this article are available online at www.sciencemag.org (this information is current as of February 25, 2014):

Updated information and services, including high-resolution figures, can be found in the online version of this article at:

<http://www.sciencemag.org/content/343/6167/171.full.html>

Supporting Online Material can be found at:

<http://www.sciencemag.org/content/suppl/2013/12/12/science.1247051.DC1.html>

A list of selected additional articles on the Science Web sites **related to this article** can be found at:

<http://www.sciencemag.org/content/343/6167/171.full.html#related>

This article **cites 58 articles**, 2 of which can be accessed free:

<http://www.sciencemag.org/content/343/6167/171.full.html#ref-list-1>

This article has been **cited by** 1 articles hosted by HighWire Press; see:

<http://www.sciencemag.org/content/343/6167/171.full.html#related-urls>

This article appears in the following **subject collections**:

Planetary Science

http://www.sciencemag.org/cgi/collection/planet_sci

Transient Water Vapor at Europa's South Pole

Lorenz Roth,^{1,2,*†} Joachim Saur,^{2†} Kurt D. Retherford,¹ Darrell F. Strobel,^{3,4} Paul D. Feldman,⁴ Melissa A. McGrath,⁵ Francis Nimmo⁶

In November and December 2012, the Hubble Space Telescope (HST) imaged Europa's ultraviolet emissions in the search for vapor plume activity. We report statistically significant coincident surpluses of hydrogen Lyman- α and oxygen OI 130.4-nanometer emissions above the southern hemisphere in December 2012. These emissions were persistently found in the same area over the 7 hours of the observation, suggesting atmospheric inhomogeneity; they are consistent with two 200-km-high plumes of water vapor with line-of-sight column densities of about 10^{20} per square meter. Nondetection in November 2012 and in previous HST images from 1999 suggests varying plume activity that might depend on changing surface stresses based on Europa's orbital phases. The plume was present when Europa was near apocenter and was not detected close to its pericenter, in agreement with tidal modeling predictions.

Europa's exceptional surface morphology suggests the existence of a layer of liquid water under the icy crust (1, 2), which has been confirmed independently by magnetometer measurements (3). Despite signs of active resurfacing in chaos terrains (4) and the existence of a subsurface ocean, current geologic activity has not been observed directly in Voyager and Galileo observations (2, 5, 6) or in any other data. Europa also possesses a tenuous atmosphere generated by sputtering and radiolysis (7–9) that was detected in 1995 through Hubble Space Telescope (HST) ultraviolet (UV) observations of O emissions at 130.4 nm and 135.6 nm (10, 11). Spatially revolved images of these atmospheric emissions obtained by the HST Space Telescope Imaging Spectrograph (STIS) revealed an irregular emission pattern at the two O multiplets, which originates from an inhomogeneous neutral gas abundance across the surface (12, 13) or Europa's highly variable plasma environment, or both. An enhanced emission near 90°W longitude detected by the HST Advanced Camera for Surveys (ACS) was associated with a possible existence of plumes in a region where high shear stresses

are expected, but an unambiguous correlation was not possible because of low data quality (14).

We report STIS spectral images of Europa's trailing/anti-jovian hemisphere and leading hemisphere obtained in November and December 2012, respectively. Previous observations, in 1999, targeted Europa's trailing hemisphere (Table 1). The observations in 2012 were timed to coincide with the maximum variation of Jupiter's magnetic field orientation at Europa. With this configuration, spatially inhomogeneous yet time-variable emissions originating from the periodically changing magnetospheric conditions can be separated from time-stationary emission inhomogeneities due to atmospheric anomalies.

After correction of the images for instrumental and background noise (15), the remaining emission sources are solar reflectance from Europa's surface, solar resonance scattering by atmospheric H and O atoms (negligible for OI 135.6 nm), and electron impact (dissociative) excitation of atmospheric species, such as O₂, O, and H₂O. To subtract the light reflected from the surface, we generated model spectral images by convolving normalized inverted visible images with a solar UV spectrum (15). Whereas the surface reflectance-corrected Lyman- α brightness is mostly consistent with a zero signal for the 1999 and November 2012 observations, a pronounced 400- to 600-rayleigh (R) (16) region is found above the limb near the south pole in the residual Lyman- α emission in the December 2012 image (Fig. 11).

The residual atmospheric O emissions at 130.4 and 135.6 nm, in contrast, cover most of Europa's disk (Fig. 1, J to O). The 135.6/130.4

ratios of 1.6 ± 0.1 (both 1999 and November 2012) and 2.1 ± 0.2 (December 2012) are consistent with previous measurements and an O₂ atmosphere with a low mixing ratio of O (10, 11). The O aurora morphologies underwent considerable variations during the ~7 hours of all observations (Fig. 2 and figs. S1 and S2). Bright OI 135.6-nm patches are found close to the poles, which appear to rock toward and away from Jupiter in correlation with the varying magnetic field orientation at Europa. The OI 130.4-nm aurora pattern roughly resembles the OI 135.6-nm pattern (I and N in figs. S1 and S2, respectively), as expected if both OI multiplets originate from electron-impact-dissociated O₂. Apparent deviations of the OI 130.4-nm morphology from the OI 135.6 emission can be attributed in part to the inhomogeneity of the higher surface reflectance at 130.4 nm. This becomes most apparent in the combined images (Fig. 1, J to L), because the time-variable atmospheric contributions are smoothed through the superposition. The generally patchy OI 130.4-nm morphology is additionally affected by the low signal-to-noise ratio (SNR) of the 130.4-nm emission (15).

We focus our analysis on the emission above the limb of Europa, which is only marginally influenced by the surface reflectance due to instrument-scattered light from the on-disk features. Above the south polar limb in the December 2012 composite images, an OI 130.4-nm enhancement of similar appearance was found in the same region as the Lyman- α enhancement (compare Fig. 1, I and L). Detectable Lyman- α and OI 130.4-nm emissions were persistently found above the southern anti-jovian limb during all five HST orbits of the December 2012 observations (Fig. 2, A to J). Bright OI 135.6-nm emissions across the entire south polar region shifted from the sub-jovian to the anti-jovian hemisphere between the first and last orbits (Fig. 2, K to O). A persistent or significant above-limb OI 135.6-nm emission surplus was not detected.

In a next step, we subdivided the region between 1 R_E (Europa radius, 1561 km) and 1.25 R_E (corresponding to an above-limb altitude of 390 km) into 18 bins spanning angles of 20° around the disk of Europa in all images (Fig. 3). The December 2012 Lyman- α image brightnesses of all pixels in limb bins 12 and 13 are 420 ± 136 R and 604 ± 140 R, which exceed the faint average limb emission of 46 R (outside the anomaly) by 2.8 and 4.0 times the propagated uncertainty (σ), respectively. The OI 130.4 emission of 59 ± 18 R in bin 13 is also significantly (2.4σ) higher than the average limb emission of 16 R, and bin 12

¹Southwest Research Institute, San Antonio, TX, USA. ²Institute of Geophysics and Meteorology, University of Cologne, Germany. ³Department of Earth and Planetary Science, The Johns Hopkins University, Baltimore, MD, USA. ⁴Department of Physics and Astronomy, The Johns Hopkins University, Baltimore, MD, USA. ⁵NASA Marshall Space Flight Center, Huntsville, AL, USA. ⁶Department of Earth and Planetary Sciences, University of California Santa Cruz, CA, USA.

*Corresponding author. E-mail: lorenz.roth@swri.edu

†These authors contributed equally to this work.

Table 1. HST/STIS G140L observations of Europa's UV emissions.

Observation start date and time	HST orbits/exposures	Total exp. time (min)	Spatial resolution (km/pixel)	Sub-observer W long. (°)	System III longitude (°)	Mag. lat. range (°)	True anomaly <i>f</i> (°)	Water vapor detected
5 Oct. 1999 8:39*	5/9	156	71.5	245–274	300–158	–9.5 to 6.8	343–13	No
8 Nov. 2012 20:41†	5/10	183	73.9	209–238	25–243	–9.3 to 9.5	289–318	No
30 Dec. 2012 18:49†	5/9	164	74.9	79–108	0–218	–9.5 to 9.5	185–218	Yes

*PI M. A. McGrath.

†PI J. Saur.

shows a slight enhancement (35 ± 17 R). At both lines, the emission anomaly appears to have two individual peaks in bins 12 and 13, which cannot, however, be clearly separated within the measurement uncertainties. No significant emission surplus is found in either of the bins at 135.6 nm (Fig. 3E). In 1999 and November 2012, all of the Lyman- α bins are consistent with zero signal within 2σ (17).

Detectable Lyman- α emission is not expected for the generally assumed abundance of H-bearing molecules ($\leq 10^{17} \text{ m}^{-2}$) in the global sputtered atmosphere (7–9). Lyman- α emission from a global atomic H corona that is not gravitationally bound as observed at Ganymede (18) would be isotropic. Lyman- α solar resonant scattering on atomic H also would require optically thick columns ($> 10^{17} \text{ m}^{-2}$) to produce brightnesses > 400 R and can be excluded. In contrast, H_2O freezes (19), and any enhancement must be localized to its source. In addition, electron impact on H_2O ($e + \text{H}_2\text{O}$) yields HI 121.6 nm and OI 130.4 nm, but has a lower cross section at 135.6 nm (20). Hence, the emission surplus at HI 121.6 nm and OI 130.4 nm in an area, where no remarkable enhancement of OI 135.6 nm is found, suggests a local atmospheric H_2O enhancement.

We derived average H_2O and O_2 column densities using measured cross sections for electron-impact dissociative excitation and the standard plasma parameters for Europa (15). Neglecting presumably small contributions from $e + \text{O}$ or $e + \text{H}_2\text{O}$, the observed OI 135.6-nm brightness of bin 13 requires a line-of-sight O_2 column of $\sim 5 \times 10^{19} \text{ m}^{-2}$. The Lyman- α brightness in bin 13 implies an optically thin H_2O column density of $1.5 \times 10^{20} \text{ m}^{-2}$. In this case, excitation of O_2 and H_2O would contribute 27 and 29 R, respectively, to the OI 130.4-nm emission, which is consistent with the measured brightness of 59 ± 18 R in bin 13. Thus, the Lyman- α /OI 130.4-nm/OI 135.6-nm ratios are diagnostic of $e + \text{H}_2\text{O}$ in an approach similar to the average OI 135.6-nm/OI 130.4-nm ratio being diagnostic of $e + \text{O}_2$ (10, 11).

We generated model images for two three-dimensional plume distributions, taking into account H_2O continuum absorption and resonant scattering. We started by generating a standard model for an average background atmosphere by adjusting the density of an exponentially decreasing O_2 atmosphere with low O and H_2O mixing ratios (15) to the observed OI 135.6-nm limb brightness for all observations (Fig. 3, E and F, dotted gray line). The fitted vertical O_2 column density of $N_{\text{O}_2} = 3.5 \times 10^{18} \text{ m}^{-2}$ agrees well with the observed OI 130.4 limb brightness and is consistent with previous results (7–11, 21). Deviations from the model in several bins for both O aurora lines are probably attributable to the variable plasma environment.

We then generated model images with two local H_2O plumes (15). We adjusted the plume height of 200 km and the latitudinal expansion of 10° (or ~ 270 km on the surface) to the observed spatial profile of the Lyman- α emissions. The implemented density profile resembles an intermediate case between Io's shock-dominated Pele-

type plumes (22) and the low-gravity outgassing of the Enceladus plumes (23). Because the surface source locations cannot be determined from the images, the plumes were arbitrarily centered on the anti-jovian meridian (180°W) and in the center of bins 12 and 13 at 55° and 75°S , respectively. The densities of the plumes were fit to the observed Lyman- α bin brightness, yielding total contents of 4.9×10^{31} and $8.2 \times 10^{31} \text{ H}_2\text{O}$ mol-

ecules for the plumes at 55° and 75°S , respectively. The combined plume content is one to two orders of magnitude higher than the H_2O abundance in global atmosphere models without plumes (7–9). The derived H_2O plume densities independently match the observed OI 130.4-nm emission surplus, if resonant scattering and electron impact on O with an estimated mixing ratio of $\text{O}/\text{H}_2\text{O} \sim 0.2\%$ are taken into account (15).

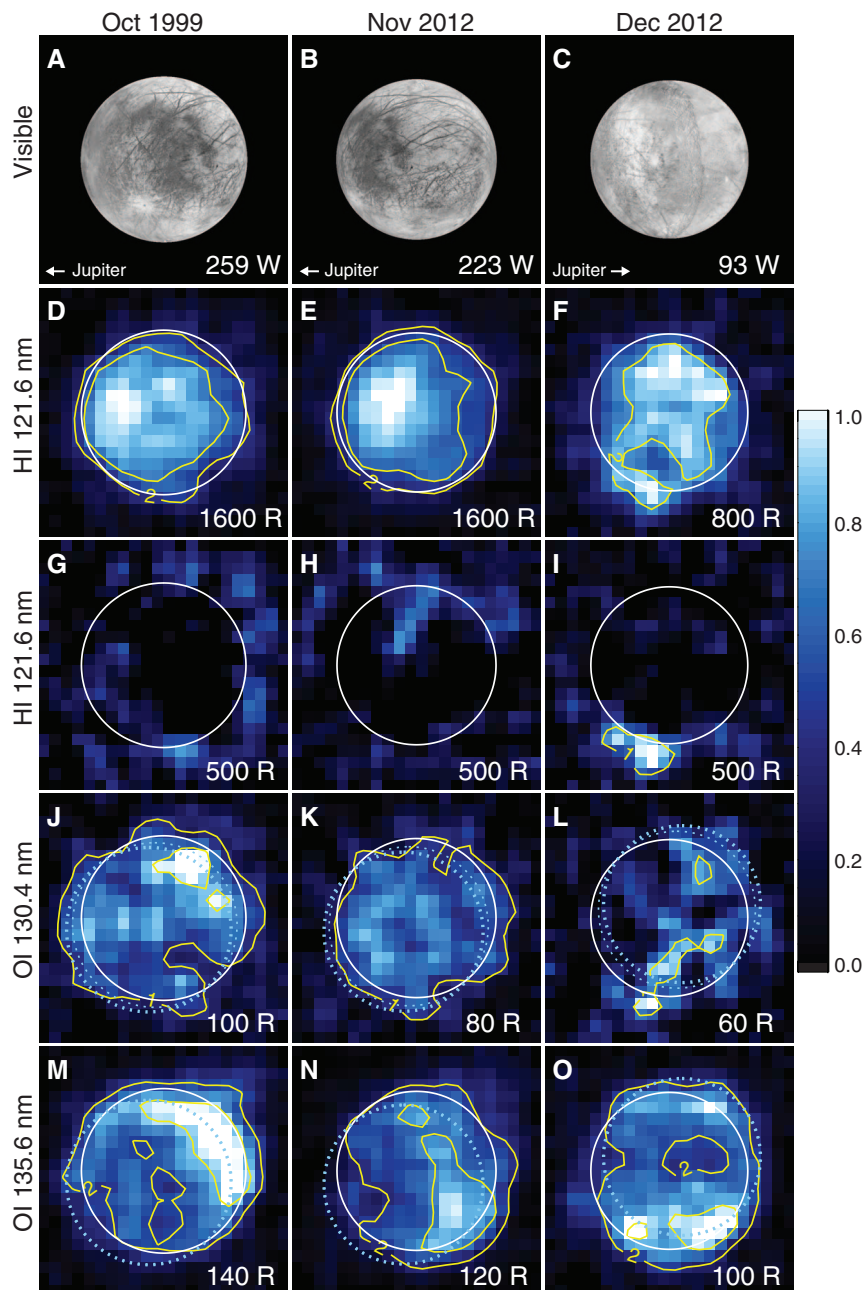


Fig. 1. Visible images of the observed hemispheres (A to C) with sub-observer longitudes listed and combined STIS images of the H and O emissions (D to O) (Table 1). The Lyman- α morphology [(D) to (F)] reveals an anticorrelation with the brightness in the visible (15). (G) to (O) Same Lyman- α images and OI 130.4-nm and OI 135.6-nm images with solar disk reflectance subtracted. 3×3 pixels are binned, and the STIS images are smoothed to enhance the visibility of the significant features. The dotted light blue circles indicate the multiplet lines (15). The color scale is normalized to the respective brightness, and the scale maximum (corresponding to 1.0 on the scale) is listed in each image. Oversaturated pixels with intensities above maximum are white. The contours show SNR ratios of the binned pixels [and contours for SNR = 1 are omitted here in (D) to (F) and (M) to (O)].

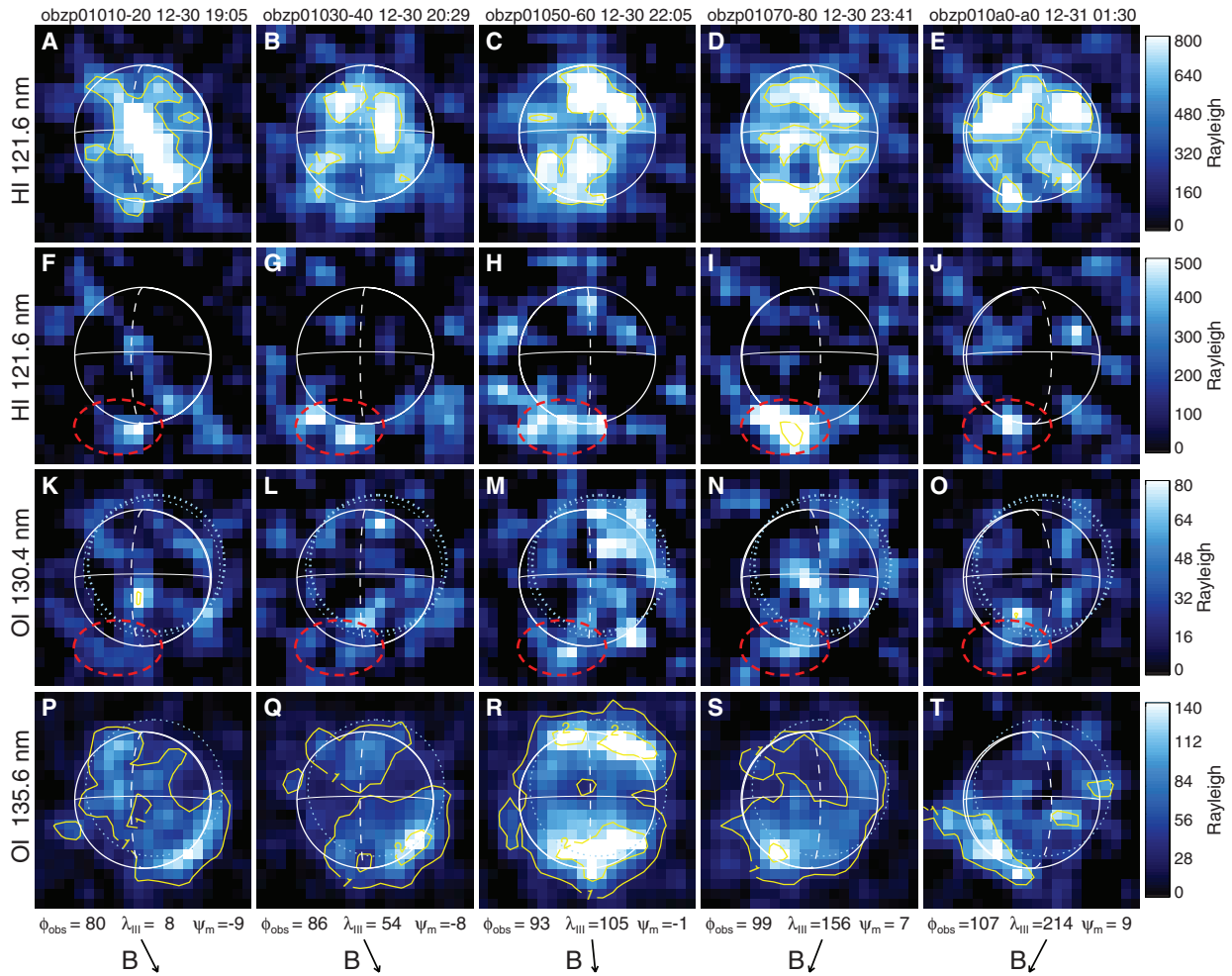


Fig. 2. Individual STIS images of the five HST orbits from December 2012. Lyman- α emissions before disk-reflectance subtraction (A to E) and reflectance-subtracted Lyman- α and O emissions (F to T). The persistent plume emission is highlighted by the dashed red circles. Sub-observer longitude ϕ_{obs} ,

jovian system III longitude λ_{III} , magnetic latitude ψ_m , and projected magnetic field line B are listed at the bottom of the figure. The leading meridian (90°W) is shown by a dashed white line, and the equator shown by a solid white line. Other details are as in Fig. 1.

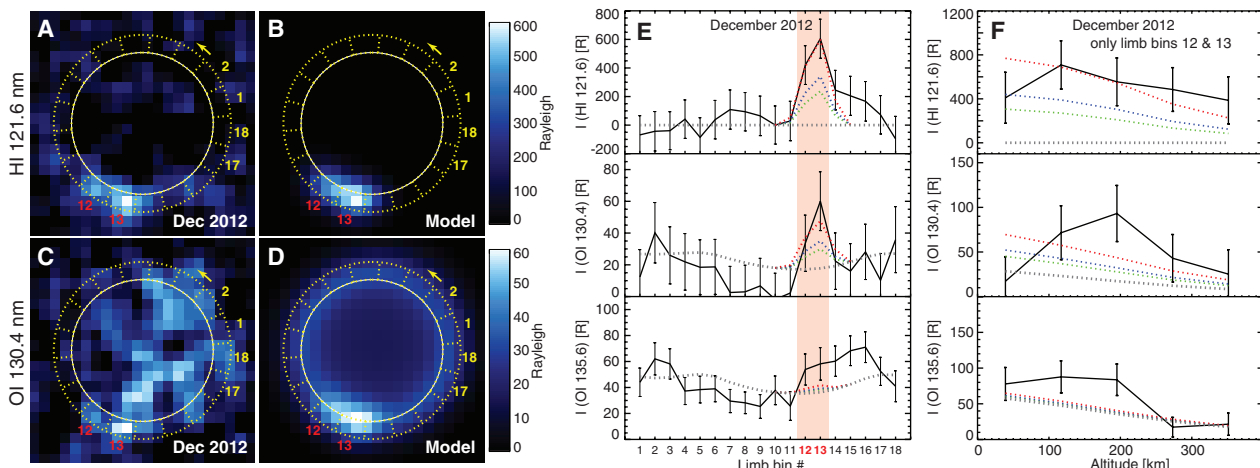


Fig. 3. Comparison of December 2012 observations and atmosphere plume model results. (A to D) Lyman- α and OI 130.4-nm STIS images (as in Fig. 1) and model aurora images from a global atmosphere with two H_2O plumes. The south polar above-limb emission is found in bins 12 and 13 (vertical shaded bar) of the 18 20° bins illustrated by the dotted yellow lines. The patchiness of the 130.4-nm on-disk emissions might originate from surface reflectance or atmospheric or plasma inhomoge-

neities, but it is also consistent with statistically expected variations across a uniform disk (15). (E) Measured (solid black line) and modeled (dotted lines) brightnesses of each 20° -wide limb bin around Europa's disk. The best-fit plume model atmosphere is shown in red, and plume densities decreased by a factor 2 and 3 are shown in blue and green, respectively. (F) Radial profiles of measured and modeled brightness versus altitude in bins 12 + 13.

The model reasonably reproduces the Lyman- α plume morphology and brightness decrease with altitude (Fig. 3). At low altitudes (<100 km), the measured brightness decreases for both the Lyman- α and OI 130.4-nm emission. Because bright OI 135.6-nm emission is also detected up to altitudes of 200 km, the OI 130.4-nm profile might be best explained by a peak in O abundance at higher altitudes. Also, the derived plume height of 200 km is higher than expected from model results (24) and would require large supersonic eruption velocities of ~700 m/s. However, interpretation of the derived height and radial profile requires caution because of the systematic uncertainties of the disk location by one or two pixels or ~100 km. Moreover, a local density enhancement within a smooth global atmosphere would substantially alter the plasma environment, which in turn modifies the aurora morphology and brightness (25).

The high plume velocities and relatively low number densities we inferred are consistent with vapor emission from narrow fractures (15), as occurs at Enceladus (23, 26). The surface area of Europa's fractures is too small to produce a thermal anomaly detectable by the Galileo Photopolarimeter-Radiometer instrument (27). Plume fallback could produce terrain softening in the near-polar regions, which might be detectable in suitable high-resolution images (15).

The modeled Lyman- α limb brightnesses for the 1999 and November 2012 geometries are not consistent with persistent plumes. Also, no striking surplus of OI 130.4-nm emission was detected. The model indicates that the plumes were less dense by at least a factor of 2 and 3 during the 1999 and November 2012 observations, respectively,

if present (fig. S3). Thus, the plume activity appears to undergo considerable variability.

Recently, the plumes at Enceladus' south pole have been shown to be more active near the apocenter than at the pericenter (28). Similar tidal stress variability for Europa is expected to open and close its Linea features [fig. S4 (15)]. Europa was very close to its apocenter during the December 2012 observations and was shortly before and at the pericenter during the 1999 and November 2012 observations (Table 1). This causal relationship might explain the observed variability and the lack of detections in 1999 and November 2012. The plume variability, if real, verifies a key prediction of tidal-flexing models based on the existence of a subsurface ocean.

References and Notes

- M. H. Carr *et al.*, *Nature* **391**, 363–365 (1998).
- R. T. Pappalardo *et al.*, *J. Geophys. Res.* **104**, 24015–24055 (1999).
- K. K. Khurana *et al.*, *Nature* **395**, 777–780 (1998).
- B. E. Schmidt, D. D. Blankenship, G. W. Patterson, P. M. Schenk, *Nature* **479**, 502–505 (2011).
- C. B. Phillips *et al.*, *J. Geophys. Res.* **105**, 22579–22597 (2000).
- S. A. Fagents, *J. Geophys. Res.* **108**, 5139 (2003).
- V. I. Shematovich, R. E. Johnson, J. F. Cooper, M. C. Wong, *Icarus* **173**, 480–498 (2005).
- W. H. Smyth, M. L. Marconi, *Icarus* **181**, 510–526 (2006).
- C. Plainaki *et al.*, *Icarus* **218**, 956–966 (2012).
- D. T. Hall, D. F. Strobel, P. D. Feldman, M. A. McGrath, H. A. Weaver, *Nature* **373**, 677–679 (1995).
- D. T. Hall, P. D. Feldman, M. A. McGrath, D. F. Strobel, *Astrophys. J.* **499**, 475–481 (1998).
- M. A. McGrath, C. J. Hansen, A. R. Hendrix, in *Europa*, R. T. Pappalardo, W. B. McKinnon, K. K. Khurana, Eds. (Univ. of Arizona Press, Tucson, AZ, 2009), pp. 485–505.
- T. A. Cassidy, R. E. Johnson, M. A. McGrath, M. C. Wong, J. F. Cooper, *Icarus* **191**, 755–764 (2007).
- J. Saur *et al.*, *Astrophys. J.* **738**, 153 (2011).
- See the supplementary materials for more information.
- Rayleigh (R) is the column emission rate of 10^{10} photons per square meter per column per second, $1 R = 10^{10}/4\pi$ photons $m^{-2} sr^{-1} s^{-1}$.
- The 1999 Lyman- α image might hint at a plume feature in the south polar region (Fig. 1G), but is not statistically significant and is therefore not considered further.
- C. A. Barth *et al.*, *Geophys. Res. Lett.* **24**, 2147–2150 (1997).
- J. R. Spencer, L. K. Tamppari, T. Z. Martin, L. D. Travis, *Science* **284**, 1514–1516 (1999).
- O. P. Makarov *et al.*, *J. Geophys. Res.* **109**, A09303 (2004).
- J. Saur, D. F. Strobel, F. M. Neubauer, *J. Geophys. Res.* **103**, 19947–19962 (1998).
- J. Zhang *et al.*, *Icarus* **163**, 182–197 (2003).
- F. Tian, A. I. F. Stewart, O. B. Toon, K. W. Larsen, L. W. Esposito, *Icarus* **188**, 154–161 (2007).
- S. A. Fagents *et al.*, *Icarus* **144**, 54–88 (2000).
- L. Roth, J. Saur, K. D. Retherford, D. F. Strobel, J. R. Spencer, *Icarus* **214**, 495–509 (2011).
- C. J. Hansen *et al.*, *Geophys. Res. Lett.* **38**, L11202 (2011).
- J. A. Rathbun, N. J. Rodriguez, J. R. Spencer, *Icarus* **210**, 763–769 (2010).
- M. M. Hedman *et al.*, *Nature* **500**, 182–184 (2013).

Acknowledgments: This work is based on HST observations available at the NASA Mikulski Archive for Space Telescopes. Support for program number GO-13040 was provided by NASA through a grant from the Space Telescope Science Institute, which is operated by the Association of Universities for Research in Astronomy, under contract NAS5-26555; and by Verbundforschung Astronomie und Astrophysik.

Supplementary Materials

www.sciencemag.org/content/343/6167/171/suppl/DC1
Materials and Methods
Supplementary Text
Figs. S1 to S10
Tables S1 to S2
References (29–70)

10 October 2013; accepted 2 December 2013
10.1126/science.1247051

Strong Sensitivity of Pine Island Ice-Shelf Melting to Climatic Variability

Pierre Dutrieux,^{1*} Jan De Rydt,¹ Adrian Jenkins,¹ Paul R. Holland,¹ Ho Kyung Ha,² Sang Hoon Lee,² Eric J. Steig,³ Qinghua Ding,³ E. Povl Abrahamsen,¹ Michael Schröder⁴

Pine Island Glacier has thinned and accelerated over recent decades, significantly contributing to global sea-level rise. Increased oceanic melting of its ice shelf is thought to have triggered those changes. Observations and numerical modeling reveal large fluctuations in the ocean heat available in the adjacent bay and enhanced sensitivity of ice-shelf melting to water temperatures at intermediate depth, as a seabed ridge blocks the deepest and warmest waters from reaching the thickest ice. Oceanic melting decreased by 50% between January 2010 and 2012, with ocean conditions in 2012 partly attributable to atmospheric forcing associated with a strong La Niña event. Both atmospheric variability and local ice shelf and seabed geometry play fundamental roles in determining the response of the Antarctic Ice Sheet to climate.

Austral summer observations in the Amundsen Sea, West Antarctica, show that lightly modified, warm (0.5° to 1.2°C) and saline (>34.6) Circumpolar Deep Water (CDW), 2° to 4°C above the in situ freezing point, pervades a network of glacially scoured seabed troughs (1) (Fig. 1A). The CDW reaches nearby Antarctic glaciers and delivers heat to the base of their 200- to 1000-m-thick ice shelves (2–4). It is overlain by a 200- to 300-m-thick layer

of cold (–1.5°C) and fresh (salinity <34.4) Winter Water (WW, Fig. 2A) that is seasonally replenished by interaction with the atmosphere and sea ice.

Pine Island Glacier (PIG), a major outlet glacier feeding one such ice shelf, has shown apparently continuous thinning (5, 6) and intermittent acceleration (7–9) from 1973 to 2009. During this period, its ice shelf has also thinned (6, 10–12), and the reduction in buttressing driven

by oceanic melting is believed to be responsible for the changes inland. Earlier analysis indicated that a higher CDW volume and temperature in Pine Island Bay (PIB) in January 2009 caused an increase in ice-shelf melting and in the associated meltwater-driven circulation, relative to 1994 (2). The lack of subannual variability in CDW temperature during 1-year-long measurement in PIB (1) and the long-term correlation between the oceanic melting and the mass loss required to sustain thinning of the ice shelf gave the impression that the ice-ocean system had shown progressive change over the last two decades. This is consistent with a positive geometrical feedback, with oceanic melt enlarging the cavity under the ice shelf, allowing stronger circulation and further melting.

However, such ice-ocean systems are likely to be more complex. The glacier's rapid change

¹British Antarctic Survey, Natural Environment Research Council (NERC), Cambridge, UK. ²Korea Polar Research Institute, Korea Institute of Ocean Science and Technology (KIOST), Incheon, Korea. ³Department of Earth and Space Sciences and Quaternary Research Center, University of Washington, Seattle, WA, USA. ⁴Alfred-Wegener-Institute for Polar and Marine Research, Bremerhaven, Germany.

*Corresponding author. E-mail: pierre.dutrieux@bas.ac.uk